CHARACTERIZATION OF AFTERSHOCK SEQUENCES FROM LARGE STRIKE-SLIP EARTHQUAKES ALONG GEOMETRICALLY COMPLEX FAULTS

by

EMILY SEXTON

A THESIS

Presented to the Department of Earth Sciences
and the Graduate School of the University of Oregon
in partial fulfillment of the requirements
for the degree of
Master of Science

June 2018

THESIS APPROVAL PAGE

Student: Emily Sexton

Title: Characterization of Aftershock Sequences from Large Strike-Slip Earthquakes Along Geometrically Complex Faults

This thesis has been accepted and approved in partial fulfillment of the requirements for the Master of Science degree in the Department of Earth Sciences by:

Amanda Thomas	Chairperson
Alan Rempel	Member
Emilie Hooft Toomey	Member

and

Sara D. Hodges	Interim Vice Provost and Dean of the Graduate School

Original approval signatures are on file with the University of Oregon Graduate School.

Degree awarded June 2018

© 2018 Emily Sexton

THESIS ABSTRACT

Emily Sexton

Master of Science

Department of Earth Sciences

June 2018

Title: Characterization of Aftershock Sequences from Large Strike-Slip Earthquakes Along Geometrically Complex Faults

Large earthquakes often exhibit complex slip distributions and occur along non-planar faults, resulting in variable stress changes throughout the fault region. To better discern the role of stress changes and fluid flow on aftershock sequences, we examine areas of enhanced and reduced mean stress along the structurally complex strike-slip faults that hosted the 1992 Landers, 2010 El-Mayor Cucapah, and 2016 Kumamoto earthquakes. We characterize the behavior of aftershock sequences with the Epidemic Type Aftershock-Sequence Model and use the Maximum Log Likelihood method to determine the optimal set of ETAS parameter values along each fault. This study indicates that extensional areas experience greater secondary aftershock triggering and a higher density of aftershocks directly following the mainshock, which could be attributed to fluid influx. However, our results also highlight some shortcomings of the ETAS model, including high parameter correlation, and influence of catalog size and magnitude cutoff on parameter estimations.

CURRICULUM VITAE

NAME OF AUTHOR: Emily Sexton

GRADUATE AND UNDERGRADUATE SCHOOLS ATTENDED:
University of Oregon, Eugene, OR
Washington University in St. Louis, St. Louis, MO

DEGREES AWARDED:
Master of Science, Earth Sciences, 2018, University of Oregon
Bachelor of Arts, Earth and Planetary Sciences: Geophysics, 2015, Washington University in St. Louis

AREAS OF SPECIAL INTEREST:
Seismology

PROFESSIONAL EXPERIENCE:

Graduate Employee, University of Oregon, 2016-2018

GRANTS, AWARDS AND HONORS:

Weiser Scholarship, University of Oregon, 2017

ACKNOWLEDGEMENTS

I would like to thank my advisor, Amanda Thomas, for her support throughout this project. I would also like to thank my committee members, Alan Rempel and Emilie Hooft. I also appreciate Brent Delbridge's contribution to this project by sharing his ETAS code. Lastly, I am grateful for all the love and support from my family, friends, and John throughout this process.

TABLE OF CONTENTS

Chapter Page

I. INTRODUCTION 1

Motivation 4

II. METHODS 5

Stress Change 5

Aftershock Identification 7

Seismicity Rate Modeling 9

Earthquakes Evaluated 13

III. RESULTS 15

Stress Change Along Faults 15

Aftershock Identification 19

Maximum Likelihood Estimates for ETAS Parameters 22

IV. DISCUSSION 28

V. CONCLUSIONS 37

Chapter Page

REFERENCES CITED 39

LIST OF FIGURES

Figure Page

1. Displacement and mean stress change on right lateral fault steps 6
2. Bimodal distribution of nearest-neighbor distribution indicating difference between earthquake families and background earthquakes 10
3. "Spanning Tree" and "Spanning Forest" for Southern California showing distribution of families and background events in space and time . . . 11
4. Slip distribution and mean stress change associated with the 1992 Landers earthquake 16
5. Slip distribution and mean stress change associated with the 2010 El Mayor-Cucapah earthquake 17
6. Slip distribution and mean stress change associated with the 2016 Kumamoto earthquake 18
7. Maps of mainshock and aftershock locations for the Landers, El Mayor-Cucapah, and Kumamoto earthquakes 20
8. Aftershock families for all three earthquakes, plotted in the spatial-temporal domain 23
9. Error Bar Plots for MLE of ETAS parameters for $|\Delta\sigma| > 0$ 26
10. Error Bar Plots for MLE of ETAS parameters for $|\Delta\sigma| > 1$ bar 27
11. Magnitude and lambda (λ) versus time for all three earthquakes 30
12. The effect of varying parameters on the number of aftershocks with time . 31
13. The effect of constraining the α value on the plot of lambda 32
14. The maximum likelihood estimate of α as a function of catalog start time 34
15. Variation in ETAS parameter estimations for earthquake data from the JMA catalog for magnitude cutoffs of 2 and 3 35
16. Variation in ETAS parameter estimations for the 2004 Mw 6.0 Parkield earthquake for catalogs of different sizes 36

LIST OF TABLES

Table Page

1. Number of aftershocks in compressional and dilational areas following each earthquake 21

2. Maximum likelihood estimates and errors for the ETAS parameter values 25

CHAPTER I

INTRODUCTION

Faults are often comprised of multiple segments, separated by discontinuities, that behave as discrete slipping surfaces and can rupture one at a time or all at once (Segall and Pollard, 1980). One fault may contain many individual segments that have different strikes, dips, and lengths, and can be offset or intersecting. Discontinuities vary in size around the world from 100s of kilometers long on the Anatolian fault, 10s of kilometers long on the San Andreas fault, to only a few centimeters in mining fractures, and can exist on normal, reverse, and strike-slip faults (Segall and Pollard, 1980). Understanding how interactions between fault segments impact the dynamic rupture process is crucial for seismic hazard assessment. Earthquakes that rupture only small segments will do far less damage than those that propagate the entire length of the fault because seismic moment is proportional to the length of fault ruptured. Several studies have been done to determine the requirements for slip to propagate across fault discontinuities during dynamic rupture (Harris and Day, 1993; Barka and Kadinsky-Cade, 1988). There has also been plenty of work to show that some discontinuities tend to store elastic strain energy and are more likely to host large earthquakes while others are more often sites of aftershocks or earthquake swarms (Segall and Pollard, 1980; Barka and Kadinsky-Cade, 1988; Lindh and Boore, 1981; Johnson and Hutton, 1982).

Seismicity is highly interactive, and faults can respond to even subtle stress changes they acquire from rupture on neighboring faults (Stein, 2003). Most faults host regular stick slip behavior, which is characterized by cycles of stress build up and dynamic instabilities, resulting in sudden slip. Rock on either side of the fault

moves relative to each other because of large scale tectonic forces, but friction along the fault resists movement (Stein and Wysession, 2009). With time, stresses built up in the rock around the fault, causing the rock to slowly deform. On preexisting strike-slip faults, when the shear stress exceeds the frictional resistance of the fault, the fault fails and slides as an earthquake. The surrounding rock rebounds to an undeformed state, and the rupture is accompanied by a stress drop (Scholz, 2002; Stein and Wysession, 2009). However, stress that is relieved at the site of rupture does not simply disappear; it migrates to nearby areas, both farther down the fault and off the main fault (Stein, 2003). Large earthquakes alter the regional stress field, decreasing the likelihood of future rupture in some areas but increasing the likelihood of subsequent earthquakes happening elsewhere on the fault or on neighboring faults (Stein, 2003). Even a subtle increase in stress on a secondary fault resulting from a nearby earthquake can cause the strength to be overcome, causing a triggered earthquake (Stein, 2003).

Earthquakes and stress build-up happen as a cyclical pattern. Following an earthquake, there is a postseismic phase where aftershocks occur for a period of years before interseismic stress accumulation begins again. The frequency of aftershocks decays with time from thousands of events in the first day to 10 shocks or less hundreds of days later (Nur and Booker, 1972). The predictable increase in seismicity directly following an earthquake means that the stress perturbations caused by the mainshock are sufficient for triggering aftershocks (Stein, 2003). Studies have found a correlation between the number of aftershocks and change in Coulomb stress (Harris, 1998), a metric used to determine if faults are brought closer to or farther from failure. The rate of seismicity increases in areas brought closer to failure by Coulomb stress changes, and drops in areas where failure is

suppressed (Harris, 1998). This concept is often explained using Dieterich's (1994) rate/state friction theory, which says friction is a variable, not a fixed value, that changes based on the rate of movement along the fault and the fault history, or state. Therefore, faults undergo a time-dependent weakening process until they fail and slip at aftershock sites (Dieterich, 1994). However, Gomberg and Davis (1996) found that there are many competing processes with different timescales that all interact following a large earthquake, and that stresses caused by large earthquakes are not the sole cause for aftershock failure. Instead, Nur and Booker (1972) argue that a viscous element is necessary to explain the time dependent nature of aftershocks. Not all aftershocks occur immediately following the mainshock, so there must be a process that causes aftershocks to behave as a diffusive process (Bosl and Nur, 2002).

Ground water diffusion in the seismogenic zone could provide the viscous mechanism responsible for such a time dependence (Nur and Booker, 1972). Following a large earthquake, the ruptured faults become highly permeable, allowing for fluids to flow through the crust, modulated by differential stress (Sibson, 1994). Immediately after an earthquake, pore fluids act as a "shock absorber", alleviating some of the stress the earthquake imparts on the regional area (Bosl and Nur, 2002). Fluids then migrate from areas of compression to areas of dilation, causing an increase in pore pressure that is proportional to the amount of volume increase. The increase in pore pressure and decrease in friction causes the strength in dilational areas to decrease (Nur and Booker, 1972). The number of aftershocks in a unit volume under dynamic stress perturbations is proportional to the change in pore pressure in the volume (Nur and Booker, 1972). Consequently, the number of shocks per time, or aftershock frequency, in a unit

volume is proportional to the time derivative of the change in local pore pressure (Nur and Booker, 1972). Therefore, as the change in pore pressure with time decreases, the aftershock frequency decreases. This means that variations in pore pressure change could be responsible for variations in the frequency of aftershocks with time.

Motivation

The goal for this study is to better discern the role of stress perturbations on time dependent processes of aftershock sequences for large earthquakes that have ruptured multiple fault segments. We believe that mean stress change and subsequently pore fluid diffusion after a mainshock are integral for understanding aftershock sequences along faults with geometric discontinuities. Following the mainshock, stress perturbations can represent pore fluid flow because fluids migrate from areas in compression to areas in dilation. We examine spatial differences in seismicity patterns between areas of increased and decreased mean stress using a seismicity rate model. The hypothesis is that aftershocks in areas in compression will exhibit a different time dependent nature than those in areas in dilation because of the change in mean stress and fluid diffusion in the crust. We hope that these findings will help to better understand the roles of multi-segment rupture, stress change, and fluid flow on aftershock sequences.

CHAPTER II

METHODS

Stress Change

For this study, mean stress change is used as a metric for quantifying dilation and compression along fault zones as it is a function of normal stresses and is thus related to the volumetric change of pore space in the rock. Changes in mean stress can be induced by fluid influx or dissipation (Nur and Booker, 1972), and discontinuities in fault geometry can result in varying mean stress distributions. On a right-lateral fault, a left-step creates a compressional area known as a restraining step-over, shown in Figure 1(a) & (c), where the fault blocks are thrust together, often creating local upwarping, anticlines, and pressure ridges (Segall and Pollard, 1980; Barka and Kadinsky-Cade, 1988). Normal tractions on the overlapping segment ends increase and inhibit sliding (Segall and Pollard, 1980). Conversely, on a right-step on a right-lateral fault, known as a releasing step-over, shown in Figure 1(b) & (d), the area between fault segments experiences dilation and can form pull-apart basins, grabens, and sag ponds (Segall and Pollard, 1980; Barka and Kadinsky-Cade, 1988). In this case, normal tractions decrease in the releasing step-overs and facilitate sliding (Segall and Pollard, 1980).

To calculate mean stress change on each fault, we compile slip distributions for each earthquake and use the USGS Coulomb Software (Toda et al., 2005; Lin and Stein, 2004), which uses fault geometry and slip distributions to calculate strain and stress change in an elastic halfspace. The software calculates the 3D strain field along nodal points in the halfspace resulting from displacements along

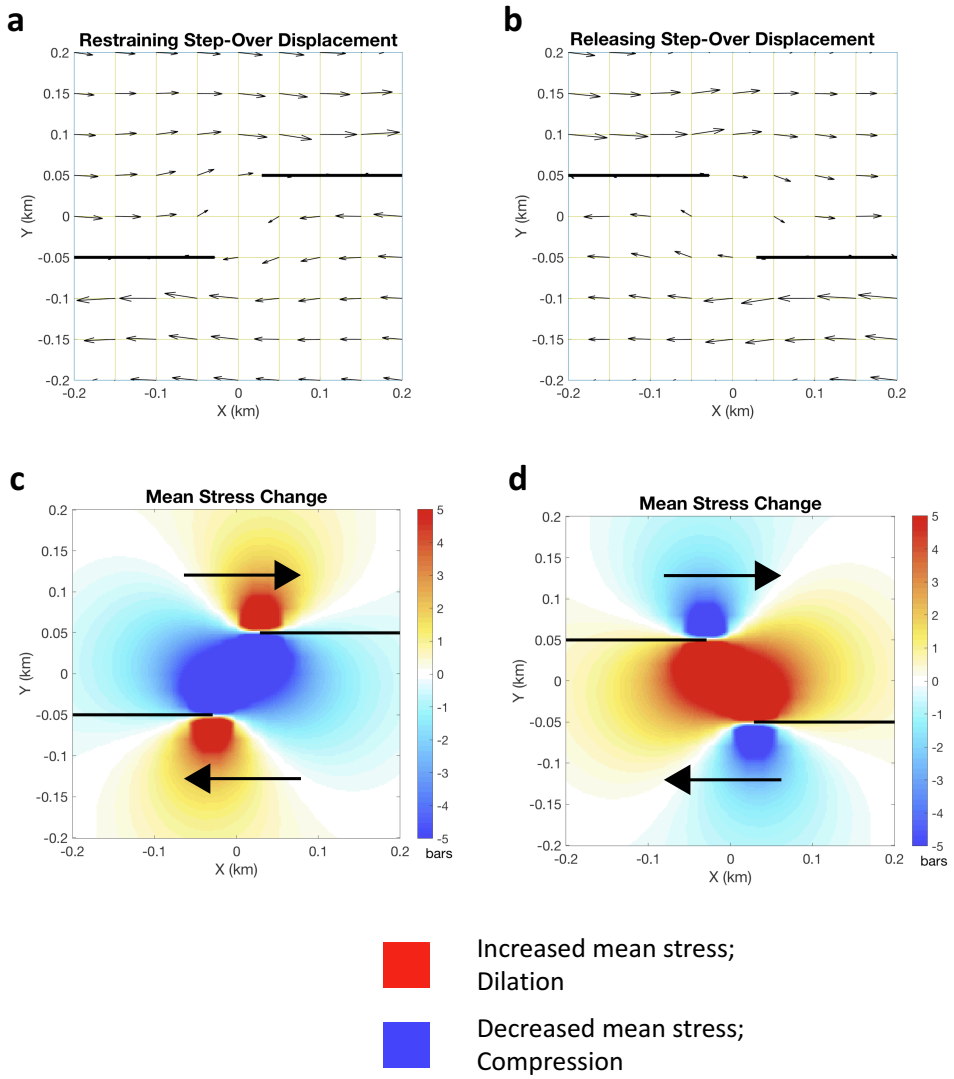


FIGURE 1. Displacement on a right lateral fault with a (a) restraining, left step and (b) releasing, right step. Corresponding mean stress change, $\frac{1}{2}(\sigma_1 + \sigma_3)$, is shown in (c) and (d) for the left and right step, respectively, where red areas represent dilation and blue areas represent compression. Fault segments in this case are vertically dipping and experience pure right-lateral slip. (a)-(d) were made with USGS′s Coulomb software (Toda et al., 2005; Lin and Stein, 2004).

the fault. Stress tensors are calculated using the constitutive equation relating stress and strain. Mean stress change is then computed using the trace of the stress change tensor:

$$\Delta\overline{\sigma} = \frac{\Delta\sigma_{11} + \Delta\sigma_{22} + \Delta\sigma_{33}}{3} \tag{2.1}$$

at each point in the area surrounding the fault. Then, we compare aftershocks in areas of positive mean stress change (dilation) and negative mean stress change (compression) to see if aftershock properties vary systematically between the two.

Aftershock Identification

To identify aftershocks of large earthquakes, we followed the methods from Zaliapin and Ben-Zion (2013). In their "nearest-neighbor approach", each event, i, is characterized by occurrence time, t_i, hypocenter (ϕ_i, λ_i, d_i), and magnitude m_i. They determine the distance N_{ij} from event j to every other earthquake i that happened before it:

$$N_{ij} = T_{ij}R_{ij} \tag{2.2}$$

T_{ij} and R_{ij} are the space and time components normalized by the parent event magnitude:

$$T_{ij} = t_{ij}10^{-qbm_i}; R_{ij} = (r_{ij})^{d_f}10^{-(1-q)bm_i} \tag{2.3}$$

where $t_{ij} = t_j - t_i$ is the inter-occurrence time between each pair of events and r_{ij} is the distance between the earthquake epicenters. The b value is the scaling parameter from the Gutenberg-Richter law, d_f is the fractal dimension of the hypocenter distribution, and q is a parameter used to define the scaled time and distance, but is not actually involved in aftershock identification. For this study,

q, b, and d_f are equal to 0.5, 1, and 1.6, respectively (Zaliapin and Ben-Zion, 2013). Minimizing the distance between an event and all other events that occurred before it yields the nearest-neighbor distance, and the event that is closest in the spatial-temporal domain is the nearest-neighbor, also known as the parent (Zaliapin and Ben-Zion, 2013). The authors observe a bimodal distribution of nearest-neighbor earthquake distances in a combined space-time-magnitude domain that separates seismic activity into two populations. The first is a population of events known as families that occur very close in space and time to their nearest-neighbor and consist of foreshocks, mainshocks, and aftershocks. The second population is background events, or singles, consisting of events that happen farther away from their nearest-neighbors (Zaliapin and Ben-Zion, 2013). Figure 2 shows the distribution of nearest-neighbor distances for earthquakes from the relocated southern California earthquake catalog from Hauksson et al. (2012). There is a bimodal distribution of events, separated by a threshold of $N_0 = 10^{-5}$. If $N_{ij} \geq N_0$, events are considered to have weak links to their nearest-neighbor and correspond to background events. If $N_{ij} < N_0$, events are strongly linked to their nearest-neighbor and are considered aftershocks. Each family has a mainshock, which is the event with the largest magnitude, foreshocks, all events that occurred before the mainshock, and aftershocks, events that occurred after the mainshock. Figure 3 illustrates events from the Hauksson et al. (2012) catalog connected to their nearest-neighbors in the space-time domain, a concept Zaliapin and Ben-Zion (2013) refer to as a "Spanning Tree". A "Spanning Forest" is also shown, where weak links have been removed, resulting in families and singles (Zaliapin and Ben-Zion, 2013). For this study, we used the Hauksson et al. (2012) relocated southern California earthquake catalog for the Landers and El Mayor-Cucapah earthquakes

and the Japan Meteorological Agency (JMA) earthquake catalog for the Kumamoto earthquake. We then applied the nearest-neighbor distance method to determine aftershocks of the large earthquakes and removed events that were more than a fault length away or after more than one day of no seismicity.

Seismicity Rate Modeling

There are multiple models used to describe seismicity rates for aftershock sequences. The modified Omori formula, also known as the Omori-Utsu formula,

$$n(t) = \frac{K}{(t+c)^p} \tag{2.4}$$

describes the frequency of aftershocks, n, at time, t, after the mainshock (t = 0) (Utsu, 1961). In this formula, K represents the aftershock productivity, or the frequency of aftershocks detected immediately after the mainshock. The c parameter is referred to as the delay constant, and corresponds to the amount of time that passes after a mainshock before all earthquakes above the magnitude of completeness are detected (Brodsky and Lajoie, 2013). Lastly, p is the rate at which aftershock activity decays with time. However, the modified Omori formula is not sufficient for describing aftershock sequences where aftershocks generate their own offspring (Omi et al., 2014). Ogata (1992) extended the modified Omori formula, proposing the Epidemic Type Aftershock Sequence (ETAS) model, a statistical model of seismicity where any earthquake can trigger secondary aftershocks, third-order aftershocks, and so on by static stress changes. The model

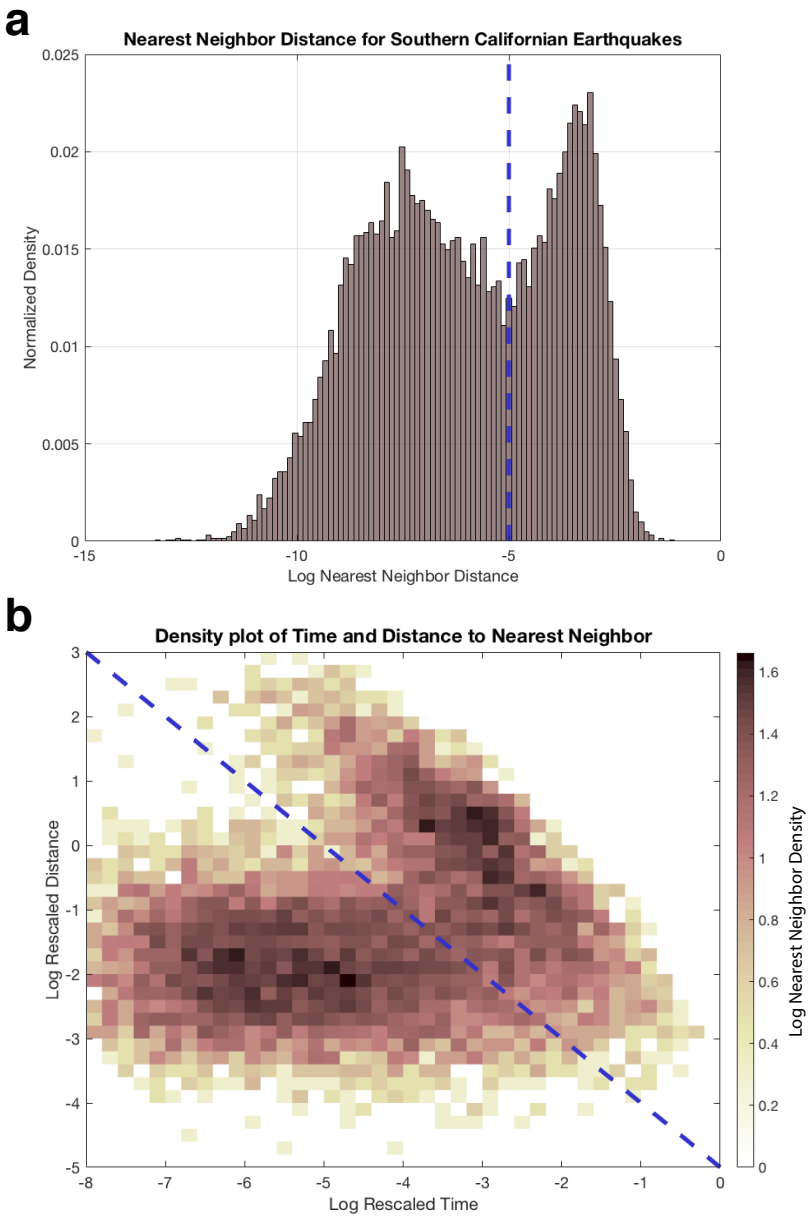


FIGURE 2. (a) Histogram of the log of the nearest-neighbor distance for all earthquakes with Mw ≥ 3 from the Southern California Relocated Earthquake Catalog (Hauksson et al., 2012) plotted against density normalized to 1, showing a bimodal distribution of seismicity. (b) Density plot of the time and distance to nearest-neighbors. The blue dashed line represents the cutoff threshold ($N_o = 10^{-5}$) where all events with $N_{ij} < N_o$ are part of families and all events with $N_{ij} > N_o$ are background events. These figures are recreations from plots from Zaliapin and Ben-Zion (2013).

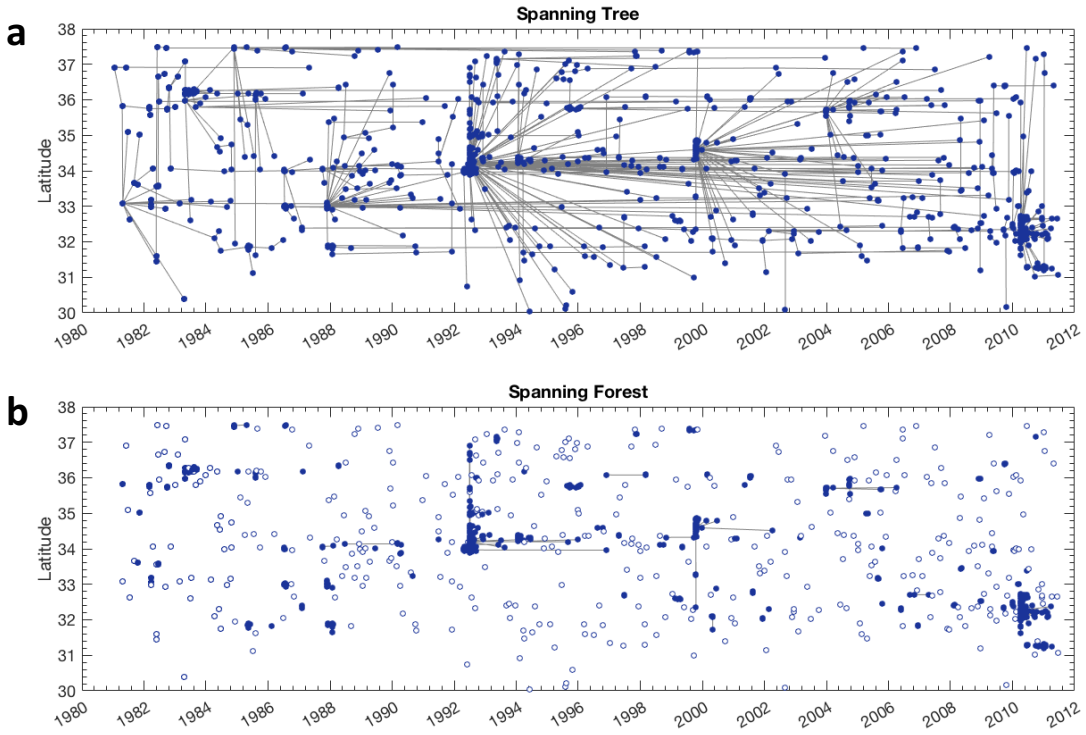


FIGURE 3. (a) The "Spanning Tree" for the Southern California Relocated Earthquake Catalog (Hauksson et al., 2012), representing all events with Mw $\geq$ 4 in the spatial-temporal domain. Each event is connected to its nearest-neighbor by a line. (b) The "Spanning Forest" for the Hauksson et al. (2012) catalog, where only families are connected by lines. Weak links ($N_{ij} \geq N_o$) have been removed and background events are shown by open circles. These figures are recreations from plots from Zaliapin and Ben-Zion (2013).

defines the seismicity rate as a function of time and is governed by the equation:

$$\lambda(t) = \mu(t) + \sum_{i:t_i<t} \frac{K}{(c+t-t_i)^p} e^{\alpha(M_i - M_{min})} \tag{2.5}$$

where $\mu(t)$ is the background seismicity rate, t_i and M_i represent the time and magnitude of events that occurred before time, t, and α is the degree of aftershock cascading, or efficiency of an aftershock at triggering other aftershocks (Omi et al., 2014). Lower values of α correspond with fewer aftershocks being generated. We use the ETAS model here to determine the time dependent nature of aftershocks in areas of positive and negative mean stress change. To estimate the ETAS model parameters, θ = (μ, K, α, c, p), for each data set, we use the log likelihood function:

$$lnL(\theta; S, T) = \sum_{i=1}^{N} ln\lambda_\theta(t_i) - \int_S^T \lambda_\theta(t)dt \tag{2.6}$$

where the observation time interval, [S,T], is the time from the mainshock to the end of the aftershock sequence (Johnson et al., 2016; Brodsky and Lajoie, 2013). We minimize the negative log likelihood function using the fmincon Matlab function. Such minimization requires making initial guesses of parameter values and setting limits that the parameters could reasonably vary between. Here, μ is held equal to zero because background seismicity has already been removed through the nearest-neighbor distance calculation. The set of parameter values that minimizes the negative log likelihood function are the most likely combination of ETAS parameter values for that catalog. One sigma errors were calculated for each parameter estimation (Ogata, 1983).

Next, we compared differences between parameter values in dilational areas versus compressional areas. In cases where parameter errors overlapped slightly,

we used a method from Ogata (1983), who uses the Akaike Information Criterion (AIC) (Akaike, 1974):

$$AIC = (-2) * max(log\ likelihood) + 2 * (number\ of\ adjusted\ parameters) \quad (2.7)$$

to discern if parameter values between two populations are the same or different. For example, to determine if K is different, two AIC values are calculated:

$$AIC_0 = (-2) * max[lnL_1(\mu, K, \alpha_1, c_1, p_1) + lnL_2(\mu, K, \alpha_2, c_2, p_2)] + 2 * (8) \quad (2.8)$$

$$AIC_1 = (-2) * [max\ lnL_1(\mu, K_1, \alpha_1, c_1, p_1) + max\ lnL_2(\mu, K_2, \alpha_2, c_2, p_2)] + 2 * (9) \quad (2.9)$$

where AIC_0 corresponds to the AIC if the parameter values in different populations are the same and AIC_1 is for parameter values that are different across the two populations. L_1 and L_2 are the likelihood functions for populations 1 and 2, or in our case the population of events that happened in dilation and the population of events that happened in compression. The AIC with the lowest value is the preferred, so if AIC_1 is lower, the parameter values are distinct, and if AIC_0 is lower, the parameter values are not significantly different.

Earthquakes Evaluated

We apply the aforementioned analysis techniques to three large strike-slip earthquakes that ruptured complex faults, the 1992 Mw 7.3 Landers, the 2010 Mw 7.2 El Mayor-Cucapah, and the 2016 Mw 7.0 Kumamoto earthquakes.

The 1992 Landers earthquake exhibited pure right lateral motion on three vertical fault segments. The rupture initiated on the Johnson Valley fault in

southern California and then propagated northward to the Homestead Valley and Camp Rock - Emerson faults. For the Landers earthquake, we use the source rupture model from Zeng and Anderson (2000) (Figure 4(a)), who inverted strong motion data from 13 nearby stations. The earthquake ruptured 70 km with a duration of 24 seconds and maximum slip greater than 6 m. Slip extended to a depth of 15 km (Zeng and Anderson, 2000).

For the 2010 El Mayor-Cucapah earthquake, we use the slip distribution from Uchide et al. (2013) (Figure 5(a)) who also inverted strong motion data from 14 local stations. The earthquake started east of Sierra El Mayor, Mexico, on a fault segment with strike and dip of 353 degrees and 56 degrees, respectively. Rupture propagated southeastwards initially, onto southwest dipping faults, and then to the northwest on faults that dip to the northeast. After 20 seconds, the rupture propagated bilaterally for a total rupture time of 52 seconds and length of about 100 km (Uchide et al., 2013). Maximum slip is about 5 m, with most of the slip concentrated to depths shallower than the hypocenter depth of 9 km (Uchide et al., 2013).

The 2016 Kumamoto earthquake initiated rupture near the intersection of the Hinagu and Futagawa faults in the central part of Kyushu Island in southwest Japan (Asano and Iwata, 2016; Fukahata and Hashimoto, 2016). We use the slip distribution from Fukahata and Hashimoto (2016) (Figure 6(a)), who inverted inSAR data to determine optimal slip distribution and dip angles of the fault. The Futagawa fault dips 61 degrees to the northwest and the Hinagu fault dips 74 degrees to the northwest, with both hosting mainly strike-slip movement. The greatest amount of slip occurred along the Futagawa fault, with slip maximum over 5 m, while the Hinagu fault had a peak displacement of only 2.4 m.

CHAPTER III

RESULTS

Stress Change Along Faults

The Landers earthquake ruptured 3 fault segments, the Camp Rock - Emerson fault to the north, the Homestead Valley fault, and the Johnson Valley fault to the south. Stress changes resulting from the mainshock (shown in Figure 4) caused dilation (corresponding to positive stress change) on the northern part of the Camp Rock - Emerson fault and off fault to the north, while compression (negative stress change) occurred to the west of the Camp Rock - Emerson fault. There is a restraining bend between the Camp Rock - Emerson fault and the Homestead Valley fault that experienced compression, with dilation to the east of the Homestead Valley fault. The Johnson Valley fault experienced mostly compression, with off fault areas in compression to the east and dilation to the west.

The El Mayor-Cucapah earthquake exhibited a complex stress change pattern, with large areas of dilation extending off the fault and smaller compressional areas localized around the faults (Figure 5). Rupture initiated near the middle of the fault system and caused dilation to the west. To the north of the rupture initiation is the Sierra Cucapah fault, which experienced dilation to the north. The Centinela fault is the northern-most segment to rupture, and experienced compression to the west. A releasing bend between the Centinela and Sierra Cucapah faults hosted extension. The fault to the south of the rupture initiation had mostly dilation to the southwest and both dilation and compression to the northeast.

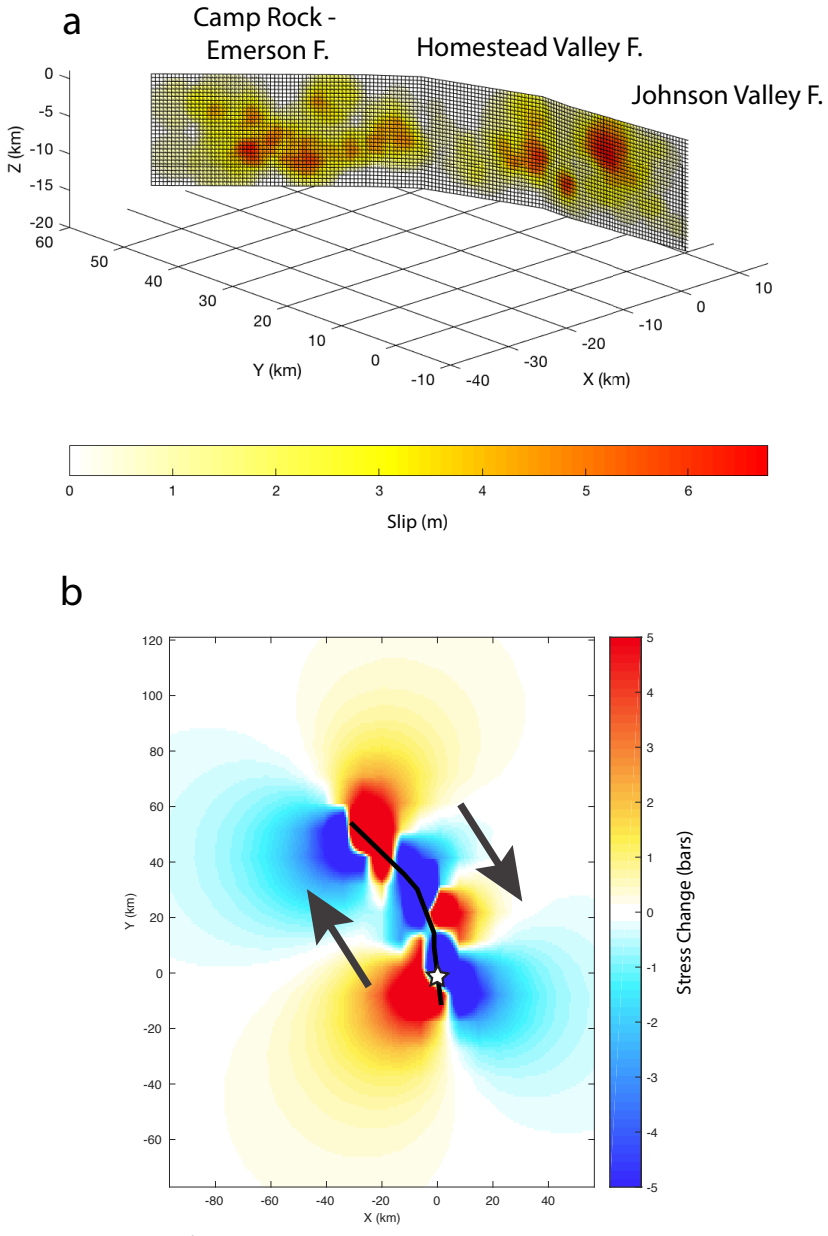


FIGURE 4. (a) Slip distribution for the 1992 Landers earthquake from Zeng and Anderson (2000), measured in meters. Red areas represent areas of maximum slip (greater than 6 m). North is in the positive Y direction and depth extends in the negative Z direction. (b) Mean stress change (in bars) calculated with the USGS's Coulomb software (Toda et al., 2005; Lin and Stein, 2004). Red zones represent dilation and blue areas correspond to compression. The rupture initiation is shown by a white star and general plate motion (right lateral) is indicated by the arrows.

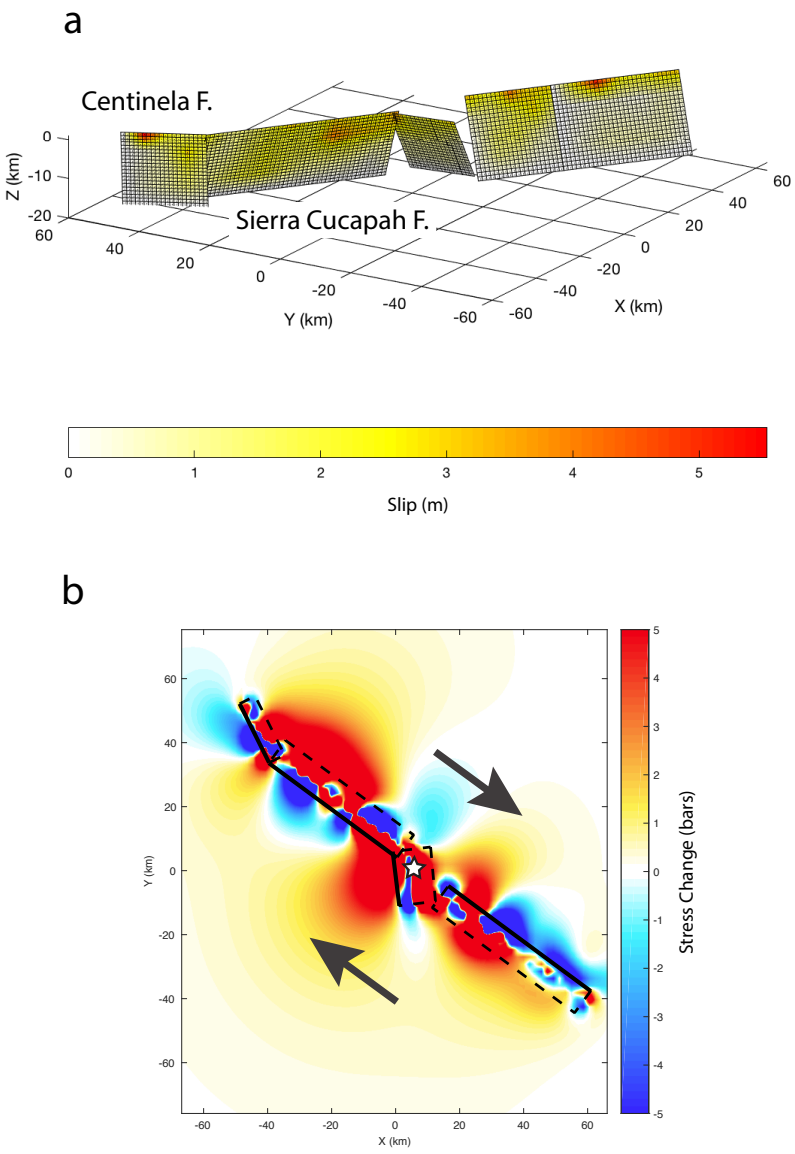


FIGURE 5. (a) Slip distribution for the 2010 El Mayor-Cucapah earthquake from Uchide et al. (2013), measured in meters. Red areas represent areas of maximum slip (greater than 5 m). North is in the positive Y direction and depth extends in the negative Z direction. (b) Mean stress change (in bars) calculated with the USGS's Coulomb software (Toda et al., 2005; Lin and Stein, 2004). Red lobes represent dilation and blue areas correspond to compression. The rupture initiation is shown by a white star and general plate motion (right lateral) is indicated by the arrows.

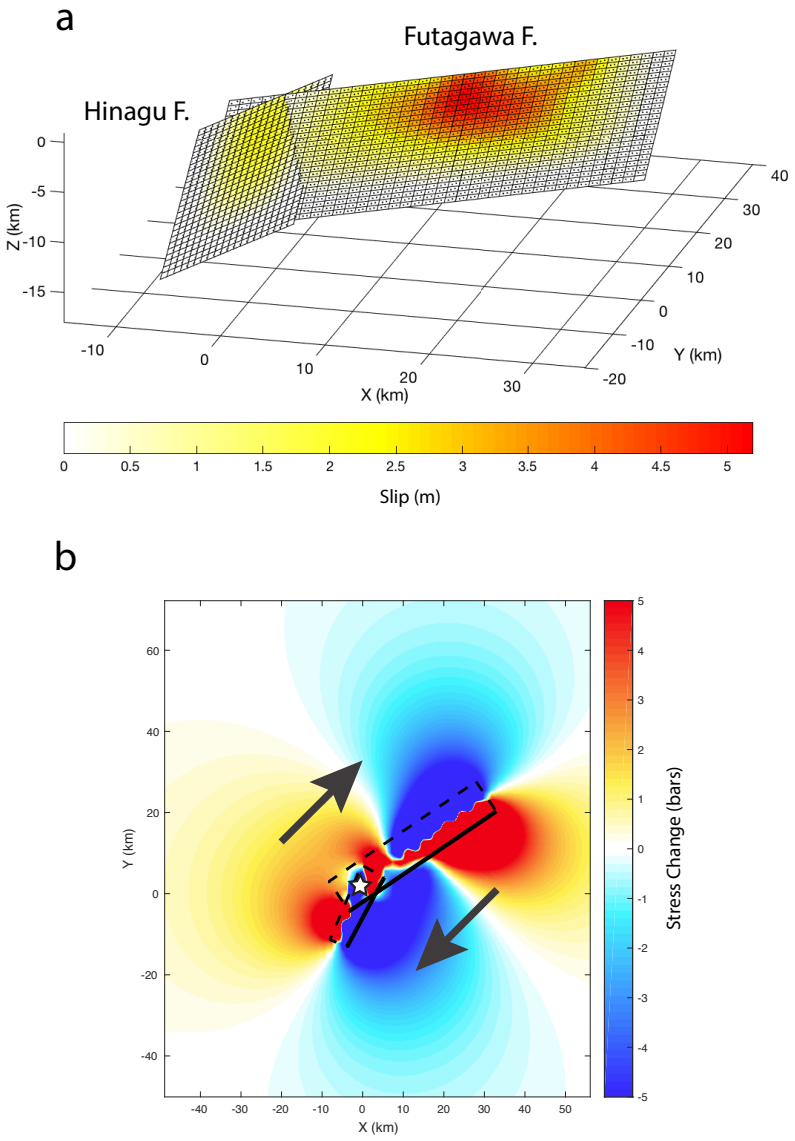


FIGURE 6. (a) Slip distribution for the 2016 Kumamoto earthquake from Fukahata and Hashimoto (2016), measured in meters. Red areas represent areas of maximum slip (greater than 5 m). North is in the positive Y direction and depth extends in the negative Z direction. (b) Mean stress change (in bars) calculated with the USGS's Coulomb software (Toda et al., 2005; Lin and Stein, 2004). Red lobes represent dilation and blue areas correspond to compression. The rupture initiation is shown by a white star and general plate motion (right lateral) is indicated by the arrows.

The mean stress distribution for the Kumamoto earthquake is shown in Figure 6. Right lateral slip along both faults resulted in compression to the north of the Futagawa fault and dilation to the east. The Hinagu fault experienced compression to the east and dilation to the west. At the intersection of the two faults, there is compression where the Futagawa fault is colliding with the Hinagu fault and dilation to the north of the intersection, where the fault segments are being pulled apart. Areas off the Hinagu fault hosted extension to the west and compression to the east.

Aftershock Identification

Aftershocks were identified for all 3 mainshocks and maps of each aftershock sequence are shown in Figure 7. Aftershocks were separated into two populations: those that occurred in areas of increased stress (dilation) and those that occurred in decreased stress (compression). We also repeated our analysis for aftershocks that only occurred in areas of large stress change ($|\Delta\sigma| > 1$ bar) to see if results differed. Table 1 displays the number of aftershocks and magnitude distribution for each population.

Initial results indicate there is no correlation between change in mean stress and number of aftershocks. For the Landers earthquake, the compressional areas host more aftershocks (2992 aftershocks for $|\Delta\sigma| > 0$ bar) than the dilational areas (2211 aftershocks). Likewise, there are more earthquakes in compressional areas (2564 aftershocks) than dilational areas (1734 aftershocks) for $|\Delta\sigma| > 1$ bar.

However, for El Mayor-Cucapah, the extensional areas host more aftershocks (1764 events) than compressional areas (1690 aftershocks) for $|\Delta\sigma| > 0$ bar. For

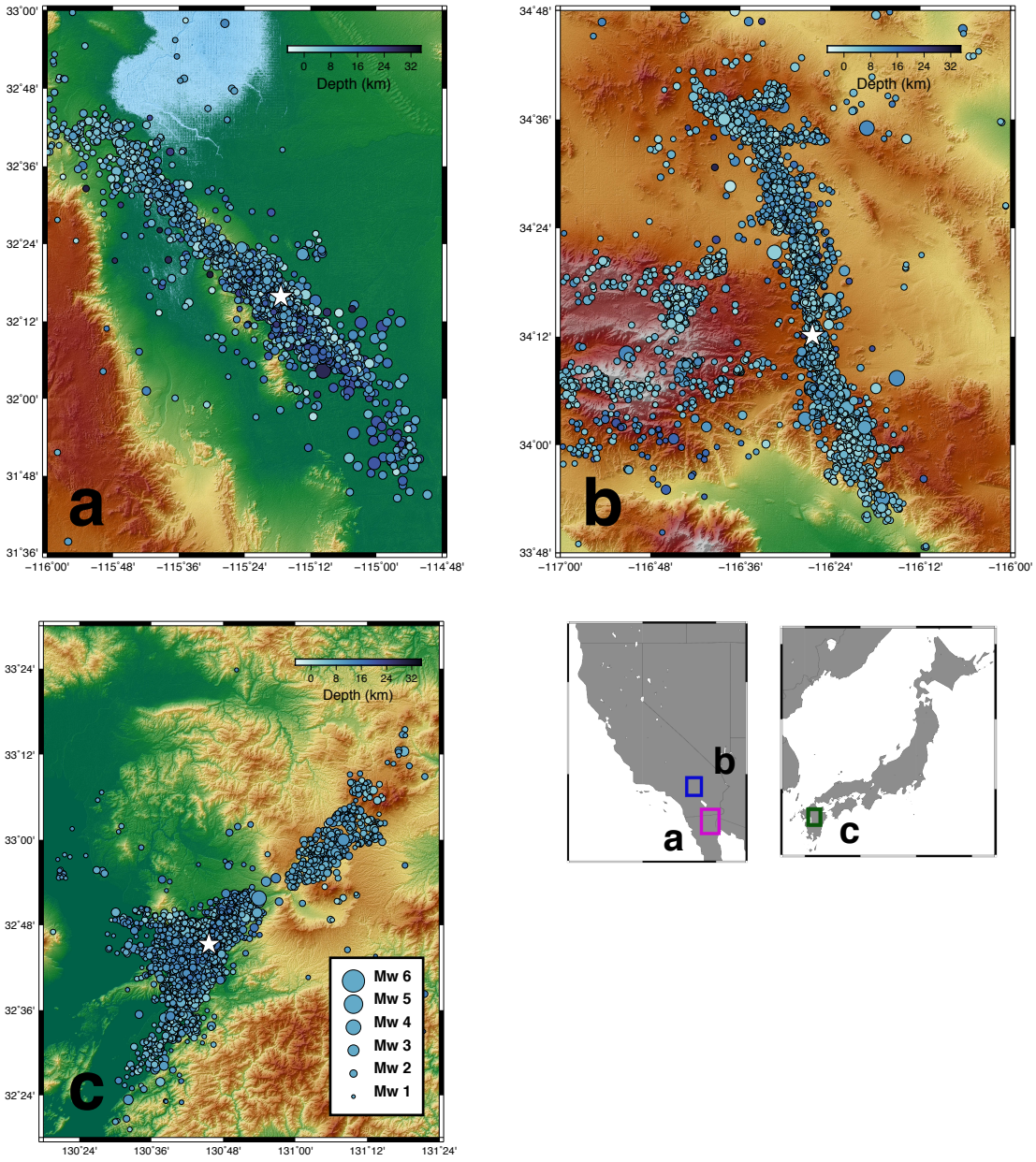


FIGURE 7. Hypocenter locations of aftershocks for the (a) 2010 El Mayor-Cucapah, (b) 1992 Landers, and (c) 2016 Kumamoto earthquakes. Circle colors and sizes represent aftershock depth and magnitude, respectively. The inset shows the circle sizes for various magnitudes. Mainshocks are depicted as white stars. Locations of boxes (a),(b), and (c) are shown in relation to California and Japan in the lower right.

	$\|\Delta\sigma\| > 0$ *bar*		$\|\Delta\sigma\| > 1$ *bar*	
	Compression	*Dilation*	*Compression*	*Dilation*
Landers				
$TotalAftershocks$	2992	2211	2564	1734
$Mag\ 2-3$	2722	1969	2338	1532
$Mag\ 3-4$	236	206	196	173
$Mag\ 4-5$	29	30	26	25
$Mag\ 5-6$	5	6	4	4
$El\ Mayor-Cucapah$				
$TotalAftershocks$	1690	1764	1371	1508
$Mag\ 2-3$	1364	1406	1088	1212
$Mag\ 3-4$	289	333	251	279
$Mag\ 4-5$	32	25	28	17
$Mag\ 5-6$	5	0	4	0
$Kumamoto$				
$TotalAftershocks$	1838	1671	1359	1378
$Mag\ 1.6-2$	725	686	500	567
$Mag\ 2-3$	887	817	685	676
$Mag\ 3-4$	204	156	154	126
$Mag\ 4-5$	21	11	20	8
$Mag\ 5-6$	1	1	0	1

TABLE 1. Number of aftershocks that occurred in compressional and dilational areas with absolute stress changes greater than 0 and 1 bar for the Landers, El Mayor-Cucapah, and Kumamoto earthquakes. The number of earthquakes of each magnitude are also shown. The Landers and El Mayor-Cucapah catalogs have $M_c = 2$ and the Kumamoto catalog has $M_c = 1.6$.

$|\Delta\sigma| > 1$ bar, there were 1371 and 1508 aftershocks in compressional and dilational areas, respectively.

Lastly, Kumamoto has more aftershocks in compressional areas (1838) than dilational areas (1671) for absolute stress changes greater than zero. However, there are slightly more aftershocks in dilational areas (1378) than compressional areas (1359) when observing only aftershocks that occurred in areas of large stress change ($|\Delta\sigma| > 1$ bar). Therefore, we cannot say that the populations in either compression or dilation host more total aftershocks as the results vary between the three earthquakes. However, these observations do not take into account the total space occupied by increased or decreased stress. Perhaps we would observe different results if we looked at the number of events per unit volume. The space-time distribution of aftershocks for the Landers, El Mayor-Cucapah, and Kumamoto earthquakes are shown in Figure 8.

Maximum Likelihood Estimates for ETAS Parameters

Maximum Likelihood Estimates for the ETAS parameters for aftershock subcatalogs containing events in compressional areas and dilational areas are shown in Table 2. Both subcatalogs for $|\Delta\sigma| > 0$ and $|\Delta\sigma| > 1$ bar were evaluated. Error bar plots of ETAS parameters are shown in Figures 9 and 10 for $|\Delta\sigma| > 0$ bar and $|\Delta\sigma| > 1$ bar, respectively.

For the Landers earthquake, subcatalogs with $|\Delta\sigma| > 0$ bar have similar c values for compressional and extensional areas and the p value is higher in areas being compacted. The K value is higher in compressional areas, but with errors overlapping quite a bit. The α value is higher in areas experiencing dilation with slightly overlapping error bars, but evaluation of the AICs from equations (2.8) and

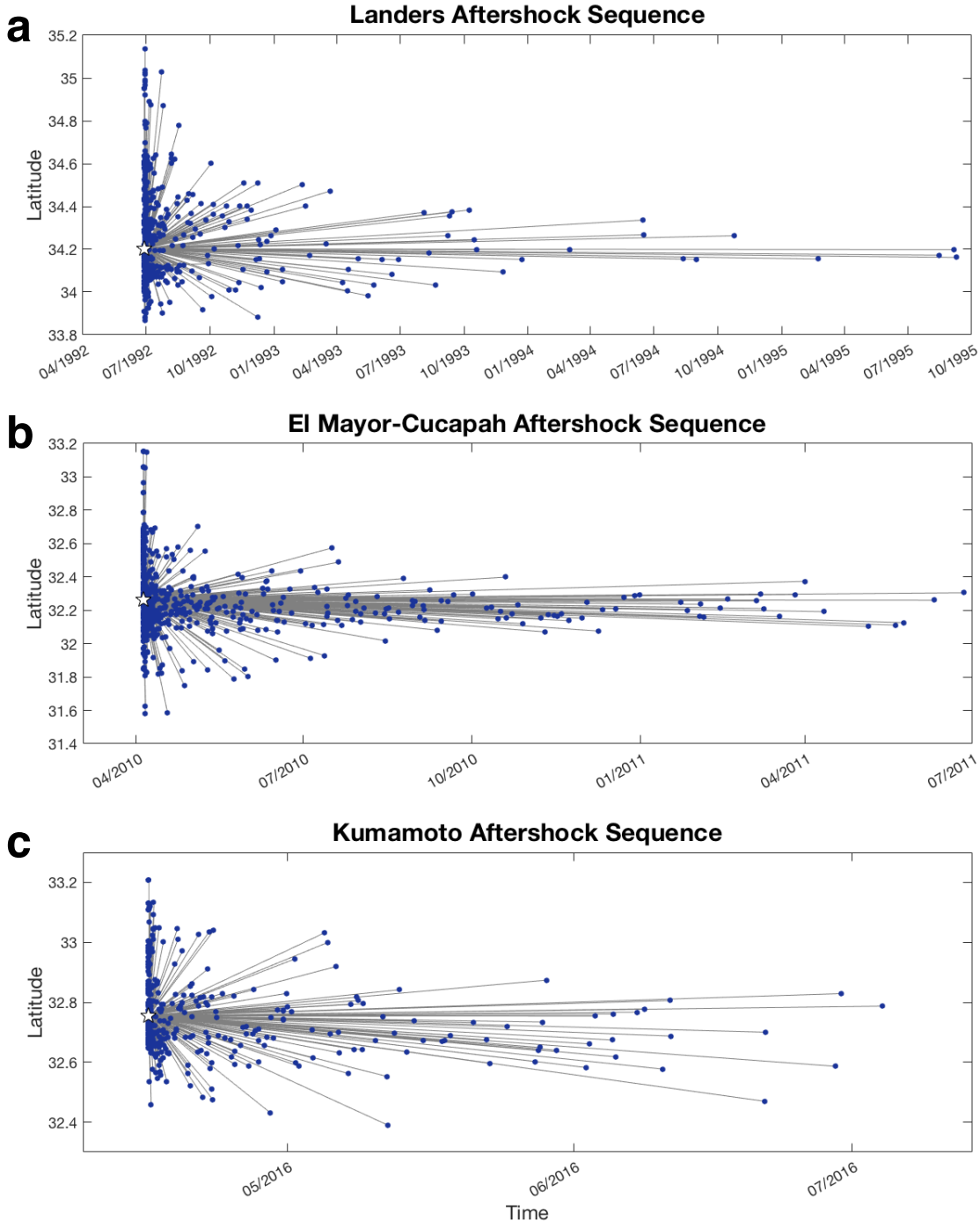


FIGURE 8. Aftershock families of events with $Mw \geq 3$ for the (a) Landers, (b) El Mayor-Cucapah, and (c) Kumamoto earthquakes in the spatial-temporal domain. Aftershocks are shown as circles and are connected to their nearest-neighbor (Zaliapin and Ben-Zion, 2013) by a line. Mainshocks are indicated by white stars.

(2.9) indicate a significant difference. Subcatalogs with $|\Delta\sigma| > 1$ bar shows similar trends for the K, α, and p parameters but in this case, c is significantly higher in extensional areas.

The El Mayor-Cucapah earthquake exhibits similar trends for the K, α, and c parameters for both subcatalogs with $|\Delta\sigma| > 0$ bar and $|\Delta\sigma| > 1$ bar. For this earthquake, there is no difference between K values in areas of increased and decreased stress. However, both α and c are are higher in dilational areas than compressional areas. The p value is higher in dilational areas for $|\Delta\sigma| > 0$ and $|\Delta\sigma| > 1$ bar but with large overlapping errors.

The Kumamoto earthquake exhibits similar results for subcatalogs with $|\Delta\sigma| > 0$ bar and $|\Delta\sigma| > 1$ bar. In both cases, the K, α, and c values are higher in dilational areas than in compressional areas. The p value is higher in dilational areas for large stress changes, but there is a large overlap of the errors for $|\Delta\sigma| > 0$.

Therefore, α is consistently higher in extensional areas across all three earthquakes, regardless of the magnitude of stress change observed. For absolute stress changes greater than 1 bar, both α and c parameters are higher in dilational areas. There are no consistent trends for the K and p parameters across all three earthquakes.

	$Compression(\Delta\sigma < 0)$		$Dilation(\Delta\sigma > 0)$		$Compression(\Delta\sigma < -1)$		$Dilation(\Delta\sigma > 1)$	
	MLE	$Error$	MLE	$Error$	MLE	$Error$	MLE	$Error$
Landers								
K	0.0804	0.00335	0.0765	0.00363	0.0841	0.00370	0.0776	0.00448
α	0.157	0.0265	0.207	0.0253	0.151	0.0279	0.258	0.0253
c	0.00496	0.00125	0.00587	0.00136	0.00549	0.00144	0.0106	0.00282
p	1.19	0.0142	1.16	0.0137	1.18	0.0148	1.15	0.0163
Cucapah								
K	0.0660	0.00473	0.0620	0.00509	0.0645	0.00541	0.0657	0.00580
α	0.276	0.0284	0.369	0.0267	0.324	0.0295	0.384	0.0262
c	0.0126	0.00443	0.0300	0.00984	0.00599	0.00220	0.0182	0.00713
p	1.12	0.0219	1.15	0.0293	1.13	0.0256	1.15	0.0300
Kumamoto								
K	0.0532	0.00306	0.0586	0.00343	0.0540	0.00376	0.0619	0.00385
α	0.215	0.0279	0.275	0.0263	0.208	0.0333	0.284	0.0290
c	0.000323	9.22e-05	0.00254	0.00129	1.89e-04	6.78e-05	0.00637	0.00251
p	1.12	0.0139	1.15	0.0331	1.10	0.0140	1.20	0.0358

TABLE 2. Maximum likelihood estimates and errors for the ETAS parameter values, $\theta = (k, \alpha, c, p)$, for areas in compression and dilation for all 3 earthquakes. Calculations were completed for both $|\Delta\sigma| > 0$ bar and $|\Delta\sigma| > 1$ bar.

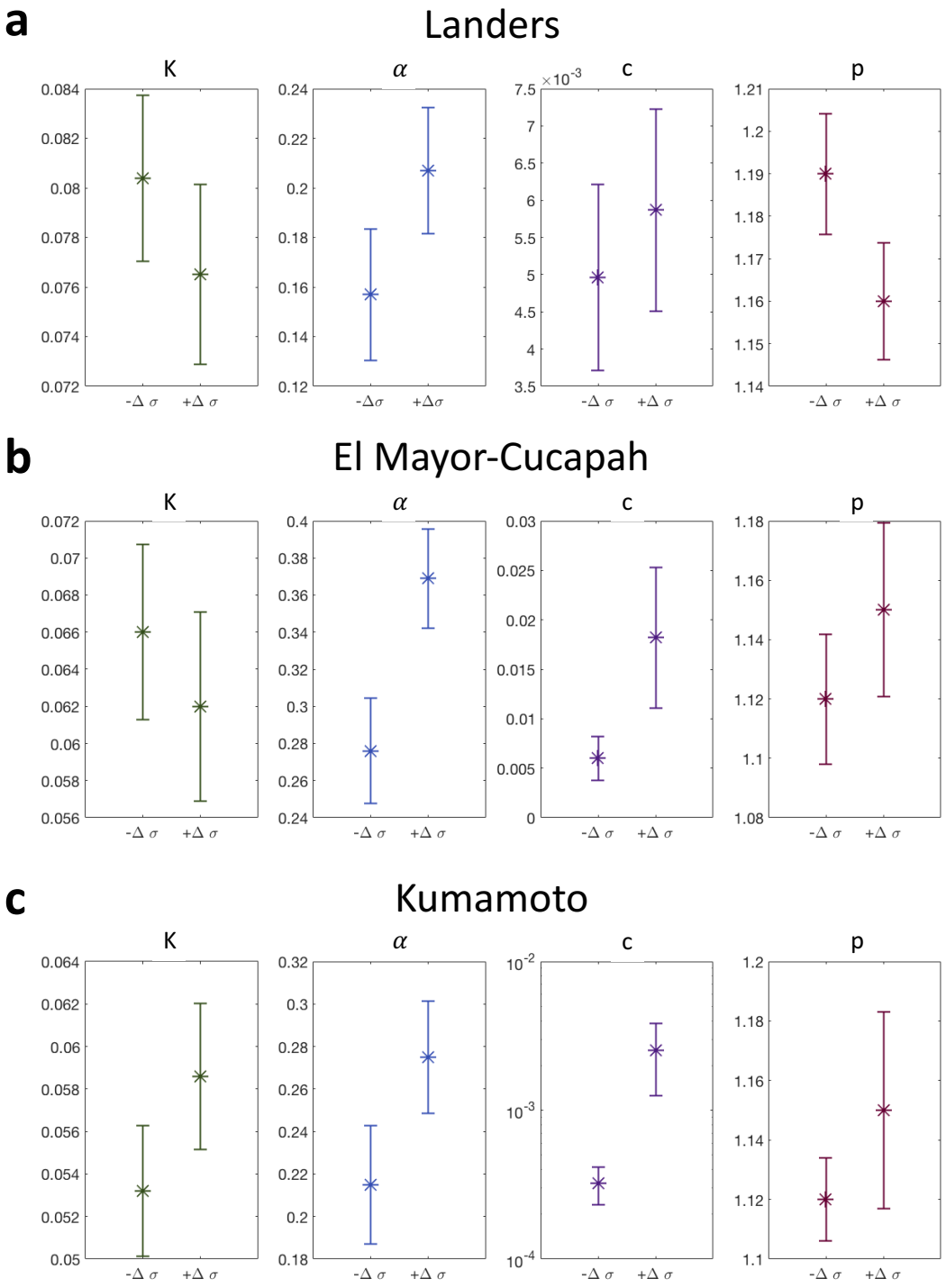


FIGURE 9. Error Bar Plots for MLE of ETAS parameters for $|\Delta\sigma| > 0$ for the (a) Landers, (b) El Mayor-Cucapah, and (c) Kumamoto earthquakes. Asterisks correspond to the maximum likelihood estimates of parameters and bars extend out to parameter error values.

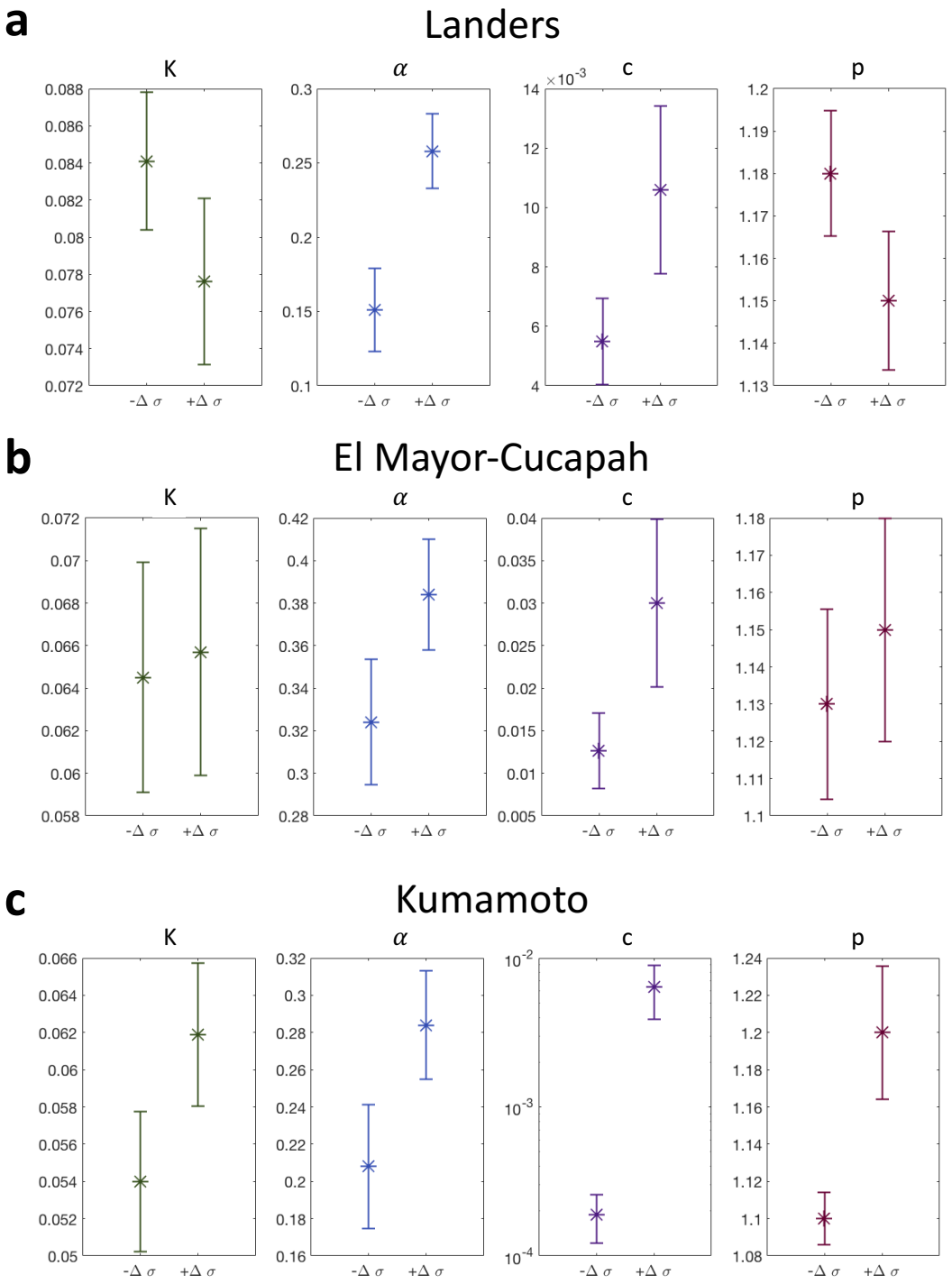


FIGURE 10. Error Bar Plots for MLE of ETAS parameters for $|\Delta\sigma| > 1$ bar for the (a) Landers, (b) El Mayor-Cucapah, and (c) Kumamoto earthquakes. Asterisks correspond to the maximum likelihood estimates of parameters and bars extend out to parameter error values.

CHAPTER IV

DISCUSSION

The motivation for this project was to determine if there are systematic differences between aftershock sequences in areas that are in compression following a large earthquake and areas that are in extension. Our hypothesis was that changes in mean stress and the flow of fluids in the ground could influence the time dependent nature of aftershocks and the ability for more aftershocks to be triggered. Such differences between aftershock sequences would manifest themselves in the ETAS parameter values ($\theta = \mu, K, \alpha, c, p$).

First, we looked at areas in compression and dilation with absolute stress change greater than 0. For all three earthquakes, Landers, El Mayor-Cucapah, and Kumamoto, the α value was higher in dilational areas than in compressional areas. This means that the ability for secondary aftershock triggering is higher in dilational areas. This could likely be attributed to the influx of fluids following stress redistribution from the mainshock which would lower the effective normal stress and the frictional strength, promoting aftershock slip. There are no systematic differences for the remaining ETAS parameters for $|\Delta\sigma| > 0$.

Next, we evaluated only the areas that had large stress changes $|\Delta\sigma| > 1$ bar. In this case, not only is the α value higher in dilational areas but the c value is higher also. The c value represents the amount of time that passes before all aftershocks larger than the magnitude of completeness are recorded (Brodsky and Lajoie, 2013). Directly following the mainshock, there is dense seismic wave overlapping that causes some earthquakes larger than the magnitude of completeness to go undetected (Omi et al., 2014). The higher the c value, the

longer the wave overlapping and under-detection of aftershocks persists. Therefore, for dilational areas to have higher c values would mean that high levels of seismicity directly after the mainshock persist for longer than in compressional areas. This could also be caused by fluids flowing into the extensional areas, encouraging slip.

For each subcatalog analyzed, we plot lambda, the number of earthquakes as a function of time (equation 2.5), using the maximum likelihood parameter estimates (Figure 11). An important aspect to note is that each plot of lambda exhibits a high variance. We would expect to see an overall decay in lambda with time, with spikes in the plot indicating large aftershocks triggering additional events. However, the plots show that lambda is highly sensitive to small fluctuations in the aftershock catalog, and may not represent the aftershock data as best as possible.

We wanted to determine the effect of each parameter on the plot of lambda versus time to resolve what was causing the high variance. We solved for lambda as a function of time (equation 2.5), varying each parameter individually and using reasonable values for the remaining parameters. The effect of varying each parameter is shown in Figure 12. The α and K parameters influence the total area under the lambda curve with higher values corresponding to a larger area under the curve, and more aftershocks overall. The p and c values are responsible for the curve smoothness, with higher p values and lower c values resulting in a less smooth plot of lambda. Our plots for lambda for this study are not very smooth, which could indicate an underestimation of the c value, or overestimation of the p value.

One of the shortcomings of the ETAS model is that there is a strong correlation between parameters, which can decrease the robustness of the parameter

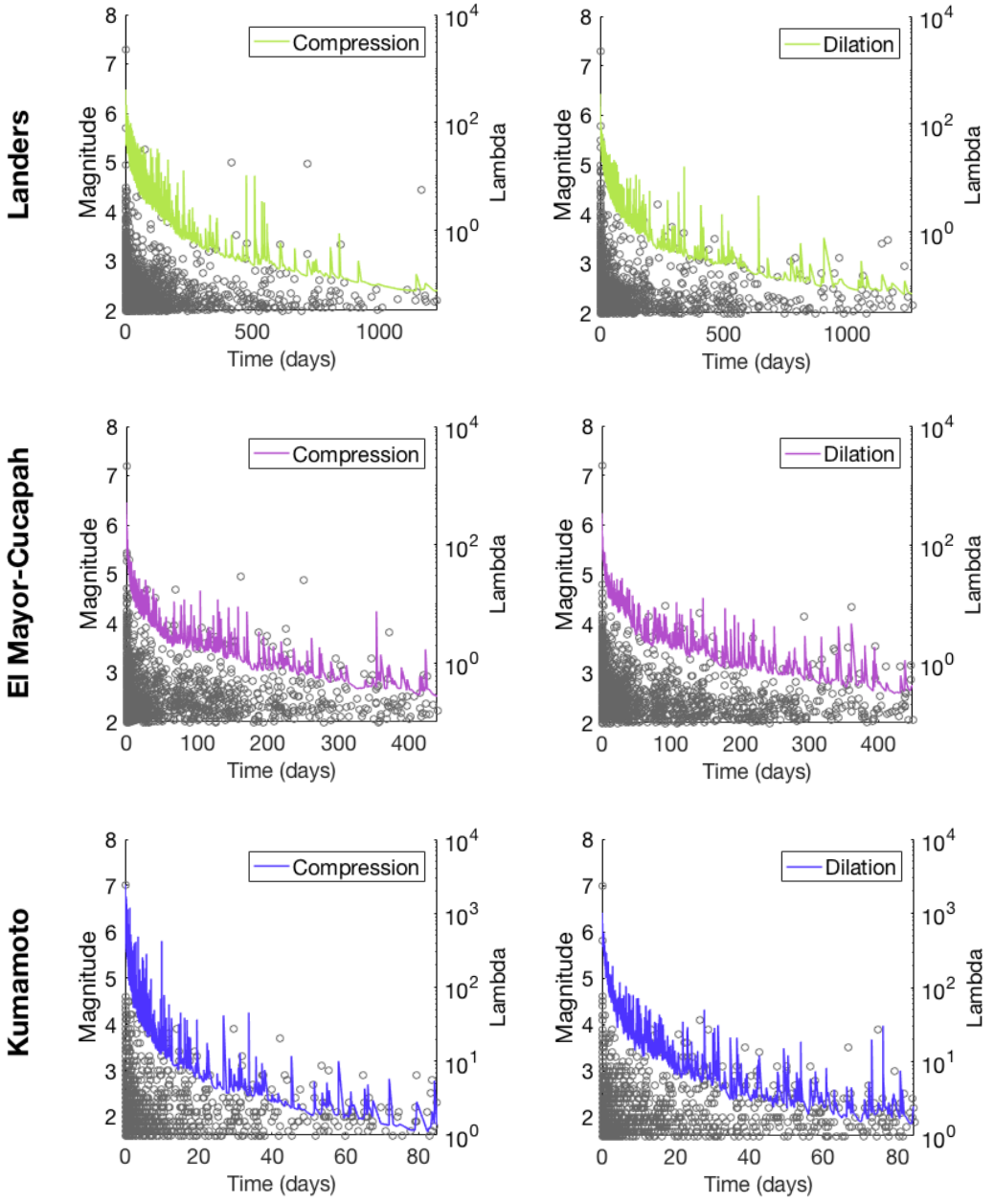


FIGURE 11. Magnitude and lambda (λ), the number of earthquakes as a function of time, plotted for all three aftershock sequences. Plots on the left are for subcatalogs of aftershocks in compression ($\Delta\sigma < -1$ bar) and plots on the right are for subcatalogs of aftershocks in dilation ($\Delta\sigma > 1$ bar). Earthquake magnitudes are plotted as gray circles and lambda is plotted as colored lines. This figure indicates that the plots for lambda are not as smooth as would be expected.

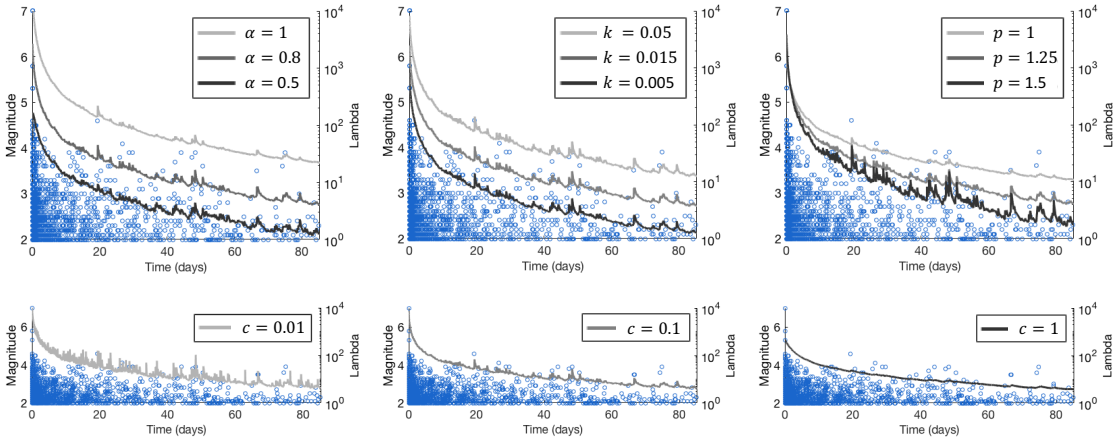


FIGURE 12. The effect of varying parameter values on lambda for the Kumamoto aftershock sequence. Aftershocks are shown as blue circles. Lambda is shown as gray lines, changing as each parameter is varied individually. As α and k increase, the total number of aftershocks increases. As p decreases or c increases, the plot of lambda as a function of time becomes more smooth.

estimation (Helmstetter et al., 2005). It is common to hold one or two of the variables constant when solving for the maximum likelihood estimate (equation 2.6) because solving for 5 free variables can often result in unreasonable solutions (Johnson et al., 2016). However, constraining one parameter value inherently influences the maximum likelihood estimates of the other parameters. Figure 13 shows the effect of constraining α on the plot of lambda. Holding α at a high value and solving for the remaining parameters makes the plot of lambda smooth. However, it was already determined that the c and p parameters are responsible for the smoothness of the plot, not the α value. Therefore, constraining one parameter while solving for the maximum likelihood estimate can influence the estimates for the other parameters, so it is important to know the value of a parameter before holding it constant. It is possible that our model has underestimated the alpha value, which would in turn affect the other parameters, creating a high variance.

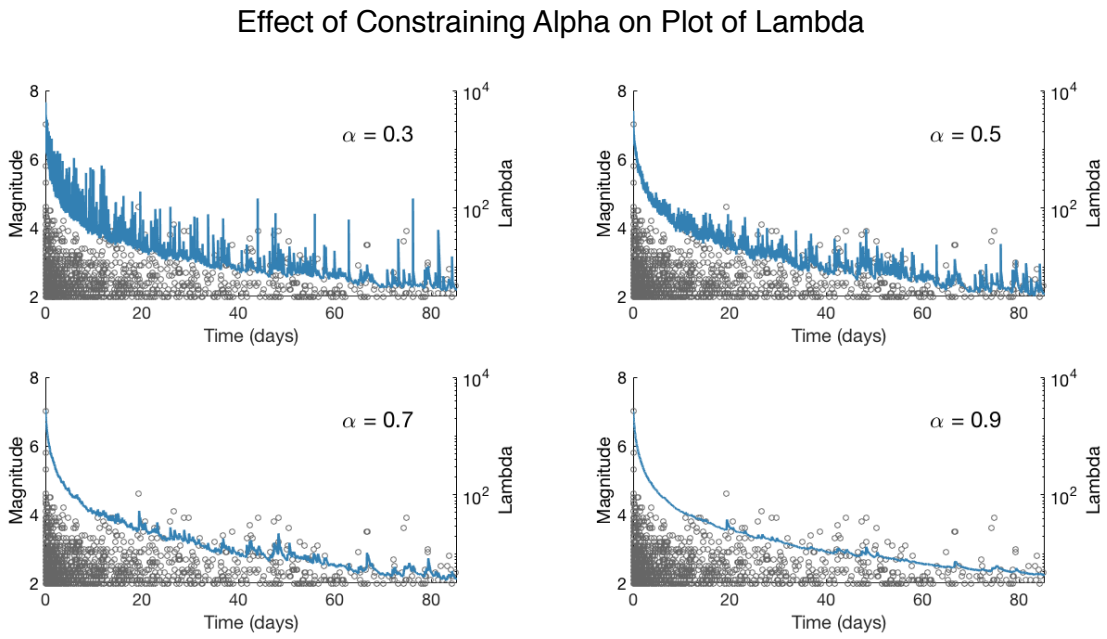


FIGURE 13. Effect of holding α value constant while solving for the maximum likelihood estimate of the remaining ETAS parameters for the Kumamoto earthquake. Aftershocks are shown as gray circles and lambda is plotted as blue lines. As α is constrained to a higher value for the maximum likelihood estimate, the plot of lambda becomes more smooth.

In an attempt to constrain a second parameter so as to only solve for three parameters, we wanted to see if α varied with time following the mainshock. The ETAS model can underestimate clustering due to temporary incompleteness in the catalog after the mainshock (Helmstetter et al., 2005; Kagan, 2004). The fact that many aftershocks go undetected immediately following the mainshock causes a deficiency in the data, masking secondary aftershock activity, which can lead to difficulties in accurately estimating the α value (Omi et al., 2014). For this reason, we wanted to see if α would increase with a delayed catalog start time by removing the effects of overlapping seismic waves. The result of this inquiry is shown in Figure 14. We found that changing the start time caused α to increase slightly over the first 0.1 days but then decrease. Another method for constraining an ETAS parameter is provided by Brodsky and Lajoie (2013), who determine the c value by solving for the time when the magnitude of completeness of the aftershock sequence converges on the catalog′s magnitude of completeness. Such method requires a much larger data set than we have for this study, so we were unable to employ this method.

Lastly, we found that the cutoff magnitude and catalog size can influence the maximum likelihood estimate of the ETAS parameters. We fit the ETAS model to earthquake data from the JMA catalog and found that using a cutoff magnitude of 2 resulted in different parameter estimates than a cutoff magnitude of 3. Parameter values and plots for lambda are shown in Figure 15. The μ, k, α, and p values were significantly different depending on if the magnitude cutoff was 2 or 3. We also tested the effect of catalog size on ETAS parameter estimates. We evaluated the Northern California Seismic Network (NCSN) catalog (137 events) for the 3 days following the 2004 Mw 6.0 Parkfield earthquake and the relocated catalog

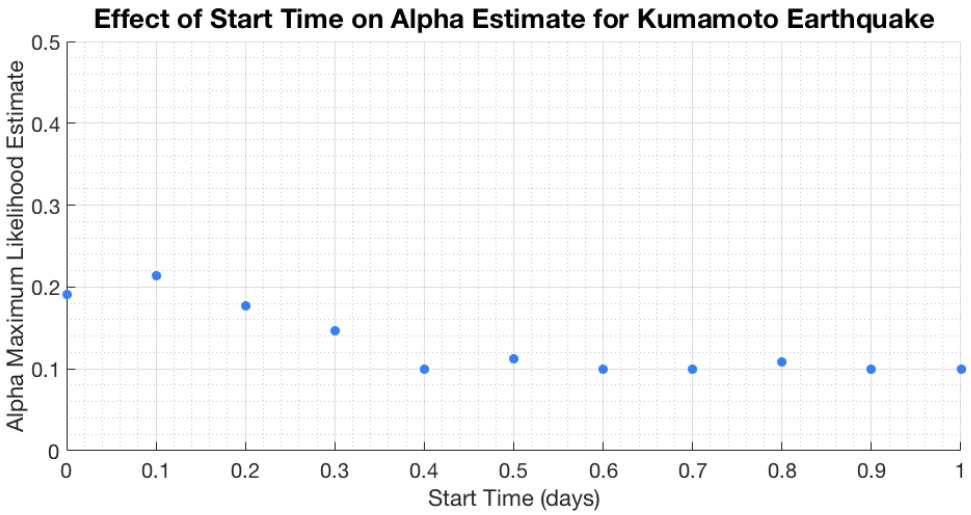


FIGURE 14. The maximum likelihood estimate of α as a function of catalog start time for the Kumamoto aftershock sequence. As catalog start time is delayed, the MLE estimate for α initially increases slightly for the first 0.1 days but then decreases.

from Peng and Zhao (2009) (319 events) for the same time after the Parkfield earthquake. Both catalogs have a magnitude cutoff of 2. We found that the α value was higher for the Peng & Zhao catalog, which has more events, but could not determine significant differences between the other parameters.

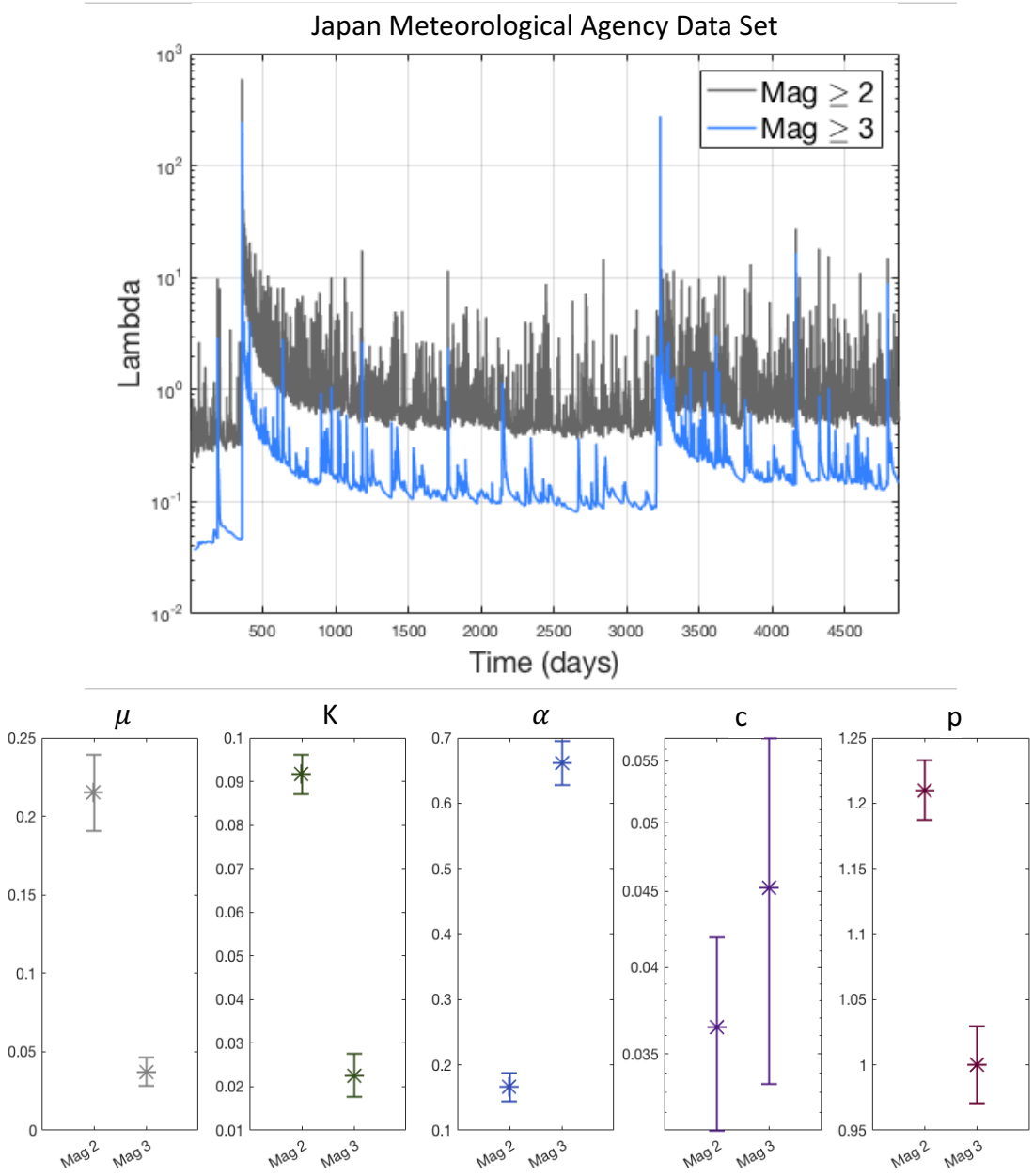


FIGURE 15. (Above) Lambda vs. time for earthquake data from the JMA catalog for a magnitude cutoff of 2 (gray line) and 3 (blue line). (Below) Error bar plots for the maximum likelihood estimates of the ETAS parameters for the different magnitude cutoffs. μ, k, α, and p values are significantly different between the two catalogs, indicating that magnitude cutoff affects the parameter estimations.

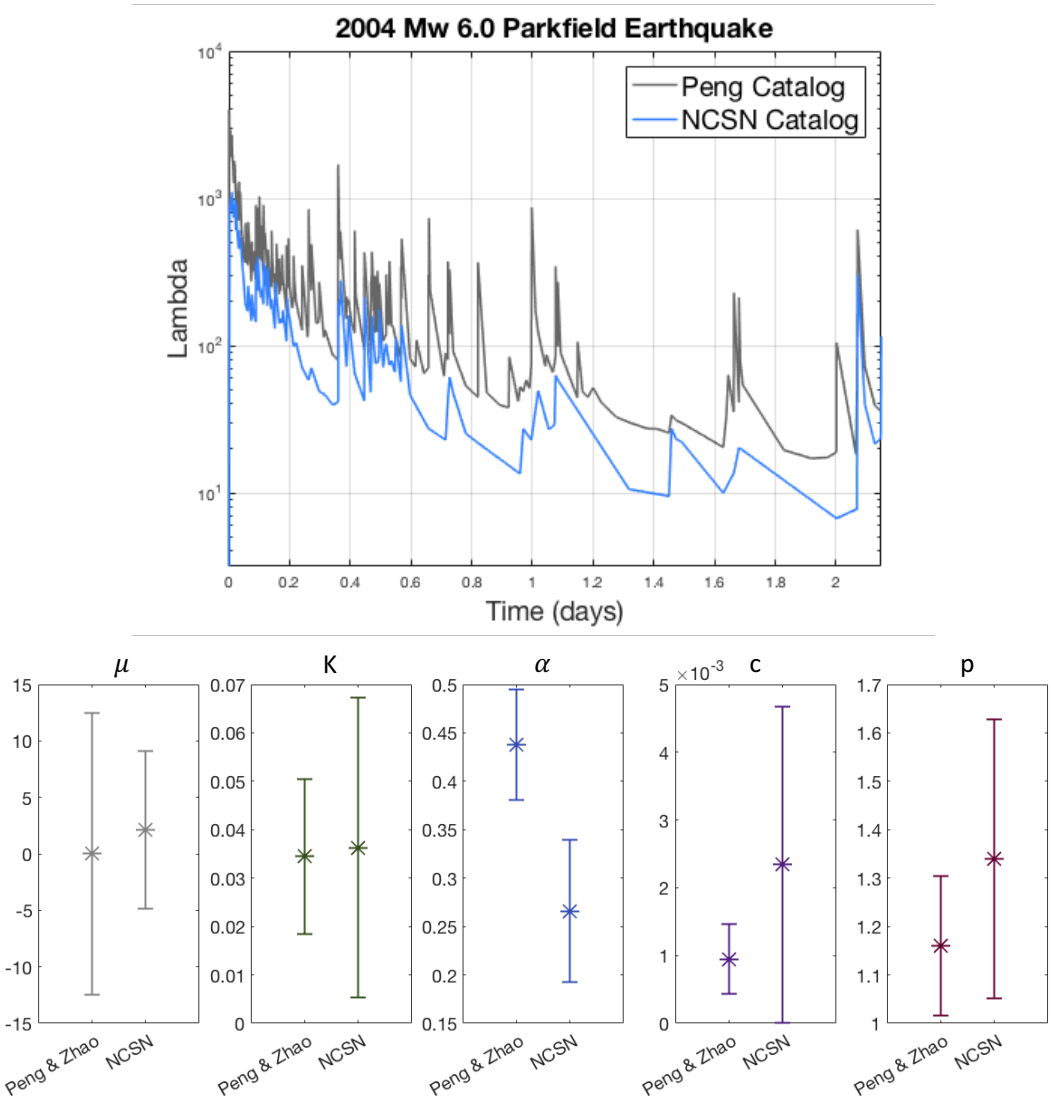


FIGURE 16. (Above) Lambda vs. time for the 2004 Mw 6.0 Parkfield earthquake for the Peng and Zhao (2009) catalog (gray line) and the Northern California Seismic Network catalog (blue line). The Peng & Zhao catalog has more than twice as many events as the NCSN catalog. (Below) Error bar plots for the maximum likelihood estimates for the ETAS parameter values for the two catalogs. The α value is significantly different between the two catalogs, indicating that catalog size could affect the α estimations.

CHAPTER V

CONCLUSIONS

This study analyzed the aftershock sequences of three large earthquakes that ruptured complex, multi-segment faults, the 1992 Mw 7.3 Landers, 2010 Mw 7.2 El Mayor-Cucapah, and 2016 Mw 7.0 Kumamoto earthquakes. The goal was to determine if aftershock sequences vary between areas of dilation (increased mean stress) and compression (decreased mean stress) following a large earthquake for $|\Delta\sigma| > 0$ and $|\Delta\sigma| > 1$ bar . We quantified differences by solving for the maximum likelihood estimates of parameters for the ETAS model for subpopulations for each earthquake. Our study resulted in the following conclusions:

- Dilational areas with stress change greater than zero had higher α values than areas in compression with stress change less than zero, corresponding to greater secondary aftershock triggering. Areas with large stress increase ($\Delta\sigma > 1$ bar) had higher α and c values than areas with large stress decrease ($\Delta\sigma < -1$ bar). The higher c value is associated with a longer time before all aftershocks above the catalog's magnitude of completeness are detected. These differences in parameter values could be attributed to the flow of fluids from compressional areas to dilational areas following a large earthquake, promoting aftershock activity in extensional areas.

- However, our maximum likelihood estimates for the ETAS parameters result in plots of λ as a function of time that are not as smooth as would be expected. We would expect to see an overall decay in lambda with time, with spikes in lambda indicating large aftershocks triggering additional

earthquakes. Our plots for lambda have numerous spikes, which may represent discrepancies between our parameter estimations and the aftershock data. This highlights flaws in the ETAS model, including high parameter correlation and our potential underestimation of the α or c values, or overestimation of the p value.

– Using a different magnitude cutoff for evaluation of the JMA catalog data resulted in dissimilar parameter estimations for 4 of the 5 ETAS parameters. Catalogs with a different number of events for the 2004 Parkfield earthquake also resulted in different α values. Thus, catalog size and magnitude cutoff could affect the estimation of ETAS parameters.

REFERENCES CITED

Akaike, H. (1974). A new look at the statistical model identification. *IEEE transactions on automatic control*, 19(6):716–723.

Asano, K. and Iwata, T. (2016). Source rupture processes of the foreshock and mainshock in the 2016 kumamoto earthquake sequence estimated from the kinematic waveform inversion of strong motion data. *Earth, Planets and Space*, 68(1):147.

Barka, A. and Kadinsky-Cade, K. (1988). Strike-slip fault geometry in turkey and its influence on earthquake activity. *Tectonics*, 7(3):663–684.

Bosl, W. and Nur, A. (2002). Aftershocks and pore fluid diffusion following the 1992 landers earthquake. *Journal of Geophysical Research: Solid Earth*, 107(B12).

Brodsky, E. E. and Lajoie, L. J. (2013). Anthropogenic seismicity rates and operational parameters at the salton sea geothermal field. *Science*, 341(6145):543–546.

Delbridge, B. G., Kita, S., Uchida, N., Johnson, C. W., Matsuzawa, T., and Bürgmann, R. (2017). Temporal variation of intermediate-depth earthquakes around the time of the m9. 0 tohoku-oki earthquake. *Geophysical Research Letters*, 44(8):3580–3590.

Dieterich, J. (1994). A constitutive law for rate of earthquake production and its application to earthquake clustering. *Journal of Geophysical Research: Solid Earth*, 99(B2):2601–2618.

Fukahata, Y. and Hashimoto, M. (2016). Simultaneous estimation of the dip angles and slip distribution on the faults of the 2016 kumamoto earthquake through a weak nonlinear inversion of insar data. *Earth, Planets and Space*, 68(1):204.

Gomberg, J. and Davis, S. (1996). Stress/strain changes and triggered seismicity at the geysers, california. *Journal of Geophysical Research: Solid Earth*, 101(B1):733–749.

Harris, R. A. (1998). Introduction to special section: Stress triggers, stress shadows, and implications for seismic hazard. *Journal of Geophysical Research: Solid Earth*, 103(B10):24347–24358.

Harris, R. A. and Day, S. M. (1993). Dynamics of fault interaction: Parallel strike-slip faults. *Journal of Geophysical Research: Solid Earth*, 98(B3):4461–4472.

Hauksson, E., Yang, W., and Shearer, P. M. (2012). Waveform relocated earthquake catalog for southern california (1981 to june 2011). *Bulletin of the Seismological Society of America*, 102(5):2239–2244.

Helmstetter, A., Kagan, Y. Y., and Jackson, D. D. (2005). Importance of small earthquakes for stress transfers and earthquake triggering. *Journal of Geophysical Research: Solid Earth*, 110(B5).

Johnson, C. and Hutton, L. (1982). Aftershocks and preearthquake seismicity in the imperial valley earthquake of october 15, 1979. *USGS Prof. Paper*, (1254):59–76.

Johnson, C. W., Totten, E. J., and Bürgmann, R. (2016). Depth migration of seasonally induced seismicity at the geysers geothermal field. *Geophysical Research Letters*, 43(12):6196–6204.

Kagan, Y. Y. (2004). Short-term properties of earthquake catalogs and models of earthquake source. *Bulletin of the Seismological Society of America*, 94(4):1207–1228.

Lin, J. and Stein, R. S. (2004). Stress triggering in thrust and subduction earthquakes and stress interaction between the southern san andreas and nearby thrust and strike-slip faults. *Journal of Geophysical Research: Solid Earth*, 109(B2).

Lindh, A. G. and Boore, D. M. (1981). Control of rupture by fault geometry during the 1966 parkfield earthquake. *Bulletin of the Seismological Society of America*, 71(1):95–116.

Nur, A. and Booker, J. R. (1972). Aftershocks caused by pore fluid flow? *Science*, 175(4024):885–887.

Ogata, Y. (1983). Estimation of the parameters in the modified omori formula for aftershock frequencies by the maximum likelihood procedure. *Journal of Physics of the Earth*, 31(2):115–124.

Ogata, Y. (1992). Detection of precursory relative quiescence before great earthquakes through a statistical model. *Journal of Geophysical Research: Solid Earth*, 97(B13):19845–19871.

Omi, T., Ogata, Y., Hirata, Y., and Aihara, K. (2014). Estimating the etas model from an early aftershock sequence. *Geophysical Research Letters*, 41(3):850–857.

Peng, Z. and Zhao, P. (2009). Migration of early aftershocks following the 2004 parkfield earthquake. *Nature Geoscience*, 2(12):877.

Scholz, C. H. (2002). *The mechanics of earthquakes and faulting*. Cambridge university press.

Segall, P. and Pollard, D. (1980). Mechanics of discontinuous faults. *Journal of Geophysical Research: Solid Earth*, 85(B8):4337–4350.

Sibson, R. H. (1994). Crustal stress, faulting and fluid flow. *Geological Society, London, Special Publications*, 78(1):69–84.

Stein, R. S. (2003). Earthquake conversations. *Scientific American*, 288(1):72–79.

Stein, S. and Wysession, M. (2009). *An introduction to seismology, earthquakes, and earth structure*. John Wiley & Sons.

Toda, S., Stein, R. S., Richards-Dinger, K., and Bozkurt, S. B. (2005). Forecasting the evolution of seismicity in southern california: Animations built on earthquake stress transfer. *Journal of Geophysical Research: Solid Earth*, 110(B5).

Uchide, T., Yao, H., and Shearer, P. M. (2013). Spatio-temporal distribution of fault slip and high-frequency radiation of the 2010 el mayor-cucapah, mexico earthquake. *Journal of Geophysical Research: Solid Earth*, 118(4):1546–1555.

Utsu, T. (1961). A statistical study on the occurrence of aftershocks. *Geophysical Magazine*, 30(4).

Zaliapin, I. and Ben-Zion, Y. (2013). Earthquake clusters in southern california i: Identification and stability. *Journal of Geophysical Research: Solid Earth*, 118(6):2847–2864.

Zeng, Y. and Anderson, J. (2000). Annual report, 1998 simulation of ground motion in the los angeles basin.